Energy Conversion and Management 293 (2023) 117445

Contents lists available at ScienceDirect

Energy Conversion and Management

journal homepage: www.elsevier.com/locate/enconman

A wind tunnel study on cyclic yaw control: Power performance and wake characteristics

Guiyue Duan, Arslan Salim Dar, Fernando Porté-Agel *

Wind Engineering and Renewable Energy Laboratory (WIRE), École Polytechnique Fédérale de Lausanne (EPFL), 1015 Lausanne, Switzerland

ARTICLE INFO

Keywords:
Cyclic yaw control
Particle-image velocimetry
Power optimization
Wake control
Wind farm
Wind tunnel experiments

ABSTRACT

In this study, wind-tunnel experiments are used to investigate cyclic yaw control as a wake mitigation strategy aiming to improve wind farm power production. The control strategy is applied to a single wind turbine and a wind farm comprising of a column of three wind turbines in full wake state. The power performance of the wind farm is optimized by adjusting the control parameters, which include the yaw angle amplitude and yaw Strouhal number, and the wake flows are investigated using particle-image velocimetry measurements. The yaw angle of the controlled turbine is varied dynamically in a sinusoidal manner. A power gain of more than 10 % compared to an uncontrolled wind farm is achieved when the yaw angle amplitude and yaw Strouhal number are in the range of 10°–35° and 0.09 – 0.22, respectively, with a peak power gain of 15.2 %. The power consumed to generate the control is found to be small and predictable. Results from wake measurements reveal that by deflecting the wake cyclically, this control strategy can lead to relatively flattened mean wake velocity deficit profiles, faster wake recovery and very different wake turbulence intensity distributions, compared to the uncontrolled case. The results show that cyclic yaw control has a great potential in improving the power production of wind farms. A scaling of the control parameters based on the kinematic similarity between the wind-tunnel scale and utility-scale wind farms is also proposed.

1. Introduction

As the world pushes towards low-carbon energy sources, wind energy is experiencing exponential growth in recent years. Conventionally, wind energy is harvested in regions with high wind resources, where wind turbines are clustered in the form of wind farms to optimize power production, land use and economic costs [1]. There is usually a trade-off between the cost of installation and the benefit in power production when considering the turbine spacing [2]. The generally used turbine spacing falls within the range of 3-10D (where D is the rotor diameter) in utility-scale wind farms [3]. Consequently, downstream wind turbines often suffer from considerable power losses and high fatigue loads owing to the wake effects of the upstream ones. Using layout optimization tools, such as the self-organizing maps [4], the genetic algorithm strategy [5] and the Monte-Carlo tree search approach [6], modern wind farms are designed to mitigate the wake effects and optimize power performance and economic costs. However, even for the optimized wind farm layouts, the wake effects cannot be eliminated. To further improve the power performance of the waked wind turbines, several wake control strategies have been proposed in the literature. These include wake steering strategies such as yaw control [7] (both passive [8] and active [9] yaw control) and tilt control [10], strategies that can accelerate wake recovery such as blade pitch control [11], and strategies that can enhance wake mixing such as axial induction control [12] and dynamic induction control whose potential has been proved in numerical simulation [13] and wind-tunnel experiments [14].

Yaw control can be considered one of the most practical and effective wake mitigation strategies, as it can reduce both power losses and structural loads on downstream wind turbines [15]. Yawing a turbine leads to wake deflection, which provides downstream wind turbines with more available power. In general, the wake deflection increases with the increase of the yaw angle and the thrust coefficient [16]. Based on a wind-tunnel study, Bartl et al. [17] achieved a 3.5 %–11 % improvement in the total power output production of two wind turbines by applying fixed yaw control (FYC) to the upstream one, the overall power gains showed a dependence on the turbulence intensity and the turbine spacing. A recent field study in an offshore wind farm reported that FYC can lead to a 4 % increase in energy production of the combined upstream–downstream turbine pair [18]. Bastankhah and Porté-Agel [7] also reported a maximum power gain of 17 % by applying FYC in a model wind farm with a column of five turbines in full wake state.

* Corresponding author.
E-mail addresses: guiyue.duan@epfl.ch (G. Duan), arslan.dar@epfl.ch (A.S. Dar), fernando.porte-agel@epfl.ch (F. Porté-Agel).

https://doi.org/10.1016/j.enconman.2023.117445
Received 26 April 2023; Received in revised form 21 July 2023; Accepted 22 July 2023
Available online 29 July 2023
0196-8904/© 2023 The Author(s). Published by Elsevier Ltd. This is an open access article under the CC BY license (http://creativecommons.org/licenses/by/4.0/).

Nomenclature

Abbreviations, notations and subscripts

CFD	Computational fluid dynamics
CYC	Cyclic yaw control
CYC-TSR	Cyclic yaw control tip-speed ratio
FOV	Field of view
FYC	Fix yaw control
PIV	Particle-image velocimetry
T1, T2, T3	Turbine 1, 2 and 3 in the wind farm model
TSR	Tip-speed ratio, or λ

Variables

γ, γ_{max}	Yaw angle and yaw angle amplitude [°]
ε	Normalized initial wake width [−]
ΔP	Power gain in the wind farm model [W]
Δu	Mean streamwise wake velocity deficit [m/s]
λ, λ_{opt}	Tip-speed ratio and the optimal tip-speed ratio [−]
ρ	Air density [kg/m^3]
σ, σ_y	Wake width (standard deviation of Gaussian fitting) and wake width in the y direction [m]
σ_u	Standard deviation of streamwise velocity [m/s]
Ω	Rotor speed [rpm]
Ω_y	Angular velocity of the yaw motion [rad/s]
A	Available power contributed by the dynamic yaw motion [−]
C(x)	Maximum mean streamwise wake velocity deficit at x [m/s]
C_{dyn}, C_{sta}	Static and dynamic contribution to the cycle-averaged available power [−]
C_P	Power coefficient [−]
C_T	Thrust coefficient [−]
D	Rotor diameter [m]
f	Yaw frequency [Hz]
I, I_0	Turbulence intensity and turbulence intensity in the baseline case [−]
I_a^{cyc}	CYC-induced added turbulence intensity [−]
I_u	Streamwise turbulence intensity [−]
$J[i,n]$	Bessel function of the first kind of order i with a variable n [−]
k	Linear wake growth rate [−]
m	Ratio between P_{yaw} and P_{To}^{base} [−]
P_a, $\overline{P}_a$	Available power and cycle-averaged available power [W]
P_{To}, P_{T1}, P_{T2}, P_{T3}	Power production of the wind farm, turbine 1, 2 and 3 [W]
P_{To}^{base}, P_{T1}^{base}, P_{T2}^{base}, P_{T3}^{base}	Power production of the wind farm, turbine 1, 2 and 3 in the baseline case [W]
P_{yaw}	Electrical power comsumed to generate cyclic yaw control [W]
R	Rotor radius [m]
R^2	Residuals squared of Gaussian fitting
S	Rotor-swept area [m^2]
St_y, St_{cri}, St_*	Yaw Strouhal number, the critical Strouhal number and the scaled yaw Strouhal number [−]
t	Time [s]
T	Cyclic yaw period [s]
u, $\overline{u}$, $\widetilde{u}$, u', u''	Streamwise velocity, time-averaged velocity, phase-averaged velocity, velocity fluctuation, and turbulent velocity [m/s]
U_∞	Streamwise inflow velocity [m/s]
$\overline{u}_c$	Wake center streamwise velocity [m/s]
u_{hub}, $\overline{u}_{hub}$	Hub-height streamwise velocity, mean hub-height streamwise velocity [m/s]
u_r	Resultant velocity [m/s]
u_*	Friction velocity [m/s]
x	Streamwise coordinate [m]
y	Spanwise coordinate [m]
$\widehat{y}$	Integration variable [m]
z_0	Roughness length [m]
z_{hub}	Turbine hub height [m]

Based on wind-tunnel experiments, Zong and Porté-Agel [9] found that FYC can lead to a peak power gain of 18 % in a model wind farm with a column of three turbines in partial wake state (the wind direction is misaligned with the turbine column by 2°–4°), which is more efficient than in the wind farm in full wake state (with a peak power gain of 5.4 %).

For practical applications, fast and accurate prediction of wake velocity distribution and power production in a wind farm under yaw control is needed. In this context, it is essential to develop analytical wake models for yawed turbines. Based on the assumption of the top-hat distribution of the average wake velocity deficit (defined as the difference between inflow velocity and wake velocity) [19], Jiménez et al. [16] proposed a model for yawed turbine wakes and compared the prediction of wake deflection between the model and large-eddy simulation data. More recently, Bastankhah and Porté-Agel [20] proposed a Gaussian model that conserves momentum in both streamwise and lateral directions and provides acceptable predictions of the wake deflection and velocity distributions in the wakes of yawed wind turbines. Recent efforts include: (1) improving the Gaussian-based model by considering the secondary wake steering effects [9] and by considering the asymmetry of wake shape [21]; and (2) developing new yawed turbine wake models such as the model based on the incompressible Reynolds-Averaged Navier-Stokes equation [22], the point vortex transportation model [23] and the vortex-sheet-based curled wake model [24].

While FYC results in deflection of the mean wake, the instantaneous wake of a turbine oscillates due to wake meandering. Wake meandering refers to a large-scale coherent fluctuation of the whole wake region in the lateral and vertical directions, which can lead to unsteady loads and power fluctuations on downstream wind turbines [25]. Wake meandering is reported to be driven by large-scale turbulent eddies in the atmospheric boundary layer (ABL) [25], especially eddies of scales larger than the wake width [26]. The amplitude of meandering motion can have an impact on the turbulent mixing and the wake recovery rate [27]. Hence enhancing the meandering motion of a turbine wake can increase turbulent mixing and accelerate wake recovery in wind farms, which can be beneficial for overall power production.

Based on a simulation study, Munters and Myers [28] reported that dynamic yaw control has a great potential in wind farm power optimization. In a recent computational fluid dynamics (CFD) simulation work by Kimura et al. [29], the authors investigated the potential of controlling the wake meandering behind a stand-alone wind turbine. The strategy is to apply dynamic yaw control on a wind turbine, in which the yaw angle varies temporally in a sinusoidal manner. Hereafter this control strategy is referred to as cyclic yaw control (CYC) in the present study. Kimura et al. [29] showed that CYC can lead to quick breakdowns of root and tip vortices, which accelerates the wake recovery by enhancing turbulent mixing between the wake and the ambient flow. A faster wake recovery results in more available energy in the wake, which can be beneficial for downstream wind turbines. It has also been reported that CYC can lead to a power increase of a stand-alone wind turbine compared to the no-control situation. This is contrary to the

previously mentioned control strategies, such as FYC and induction control, which will always cause power reduction if applied to a single turbine. Although the previous study reveals the potential of CYC in accelerating the wake recovery and improving the power performance of a single turbine, the application of this strategy in wind farm control has not been investigated comprehensively. Besides, for a sinusoidal variation of the yaw angle, the influence of the control parameters (including yaw frequency and yaw angle amplitude) on the power and wake should be examined in detail. In the present study, various combinations of CYC control parameters are tested to optimize the power output of a wind farm. Particle-image velocimetry (PIV) measurements are conducted in both the single wind turbine situation and the wind farm situation to investigate wake characteristics. To the knowledge of the authors, this is the first wind-tunnel study on CYC strategies, especially with a systematic investigation of control parameter effects.

The remainder of this paper is organized as follows. Basic information about the experimental setup, the inflow condition, the wind turbine characterization and the CYC strategy is introduced in Section 2. In Section 3, the results from both power and PIV measurements are presented and discussed. In addition, a scaling of the control parameters between the miniature and utility-scale wind farms is briefly discussed. Finally, a summary of the work and some future perspectives are given in Section 4.

2. Experimental setup and method

This section presents the details of wind-tunnel experiment setup, the miniature wind turbine and the control strategy.

2.1. Wind tunnel and inflow condition

Experiments are conducted in the boundary-layer wind tunnel of the WiRE laboratory at EPFL, Switzerland. This closed-loop wind tunnel has a 28 m long test section with a cross-section of 2.6 m in width and 2 m in height. More information regarding the wind tunnel can be found in Bastankhah and Porté-Agel [30]. In this study, the wind turbine models are placed 21 m downstream from the inlet of the wind tunnel. Owing to the long test section of the wind tunnel, a turbulent boundary layer can develop naturally without any external tripping mechanisms. The boundary layer flow upstream of the wind farm is characterized using a two-dimensional two-component PIV setup. The vertical profiles of the normalized mean streamwise velocity, streamwise turbulence intensity ($I_u = \sigma_u/\overline{u}_{hub}$, where σ_u is the standard deviation of the streamwise inflow velocity u, u_{hub} is u at the hub-height level and the overline denotes time averaging) are presented in Fig. 1. In this study, $\overline{u}_{hub} = 4.75m/s$ and $I_u = 0.07$ at the turbine hub height. By fitting the velocity profile with a logarithm law (the von Kármán constant is chosen to be 0.41), the roughness length and the friction velocity are estimated to be $z_0 = 2 \times 10^{-5}m$ and $u_* = 0.21m/s$, respectively. The ratio $z_0/D = 1.33 \times 10^{-4}$ scales to a roughness length of about 0.013 m for a full-scale turbine of 100 m diameter, which corresponds to a flat farmland terrain with cut grass [31].

2.2. Miniature wind turbine and wind farm model

The WiRE-01 model used in the experiments is a three-blade horizontal-axis miniature wind turbine with a rotor diameter $D = 0.15$m, and a hub height $z_{hub} = 0.125$m. Fig. 2 presents the power and thrust coefficients of the turbine as functions of the tip-speed ratio (*TSR*, i.e., $\lambda = \Omega R/\overline{u}_{hub}$, where Ω is the rotor rotational speed and $R = D/2$ is the radius of the rotor). During the measurements of both coefficients, the miniature wind turbine is immersed in the boundary layer with an inflow condition illustrated in Fig. 1. It is shown that at the optimal *TSR* of 3.6, the turbine reaches a maximal power coefficient C_P of 0.35, and the corresponding thrust coefficient C_T is 0.80. The power produced by

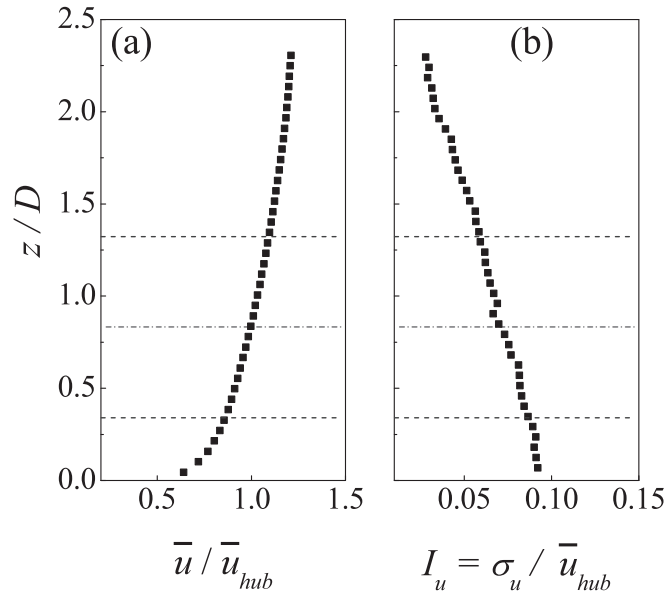

Fig. 1. Inflow condition at the test location in the empty wind tunnel: vertical profiles of (a) the normalized mean streamwise velocity and (b) the streamwise turbulent intensity. The red dash-dotted line denotes the hub height while the blue dashed lines denote the rotor top and bottom tip heights.

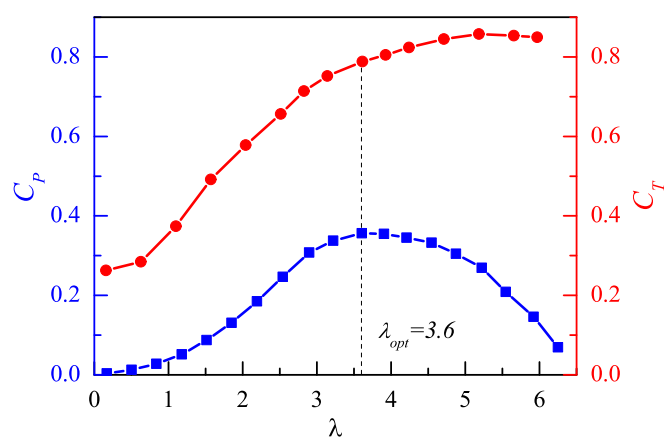

Fig. 2. The WiRE-01 miniature wind turbine: power coefficient and thrust coefficient as functions of *TSR*.

the turbine is estimated by multiplying the shaft torque with the rotational speed of the turbine. More details related to the wind turbine design, the calibration of the power, and the wind turbine performance can be found in the study of Bastankhah and Porté-Agel [32].

The wind farm model comprises of three miniature wind turbines arranged in a column aligned with the incoming wind direction, resulting in a blockage ratio of less than 0.4 %. As illustrated in Fig. 3, the streamwise spacing between two neighboring wind turbines is 5*D*. Among the three wind turbines (referred to as T1, T2 and T3 respectively as shown in Fig. 3), the tower of T1 is mounted on a step motor to enable yaw control, while no yaw control is applied to T2 and T3.

2.3. Particle-image velocimetry setup

Two-dimensional two-component PIV measurements are performed to acquire detailed wake flow information in the horizontal plane at the turbine hub height. As illustrated in Fig. 4, four fields of view (FOVs) of 3D × 4.5D (spanwise × streamwise) are set up for measurements with an overlap of 3D × 1D for every two neighboring FOVs, which means the

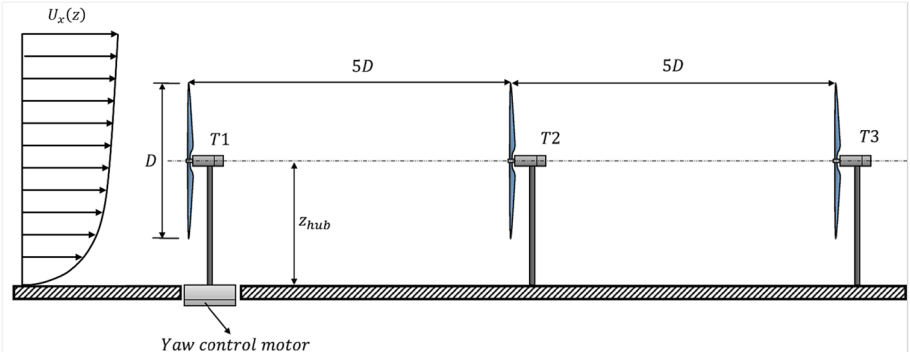

Fig. 3. Schematic of the wind farm model: side view.

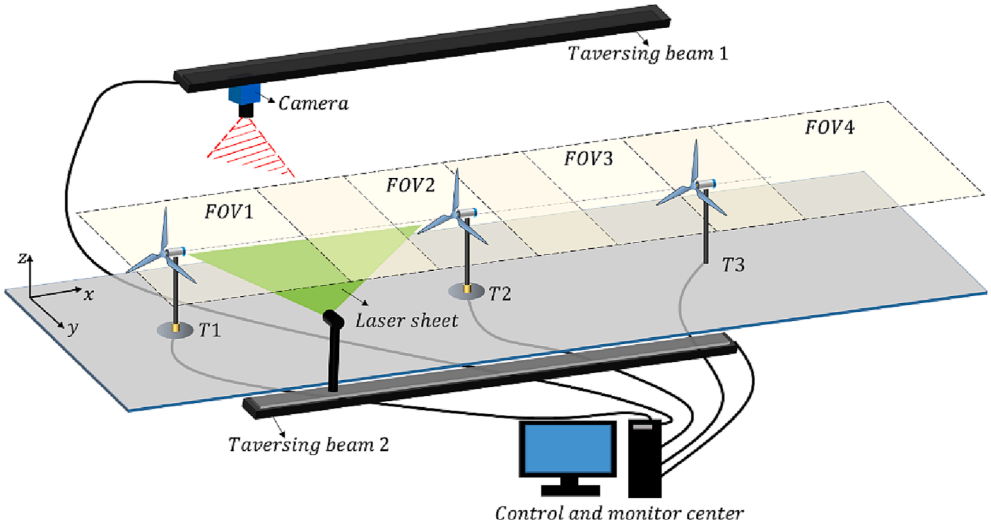

Fig. 4. Setup for PIV measurements. The four FOVs and the laser sheet are in the *xy*-plane at the hub-height level.

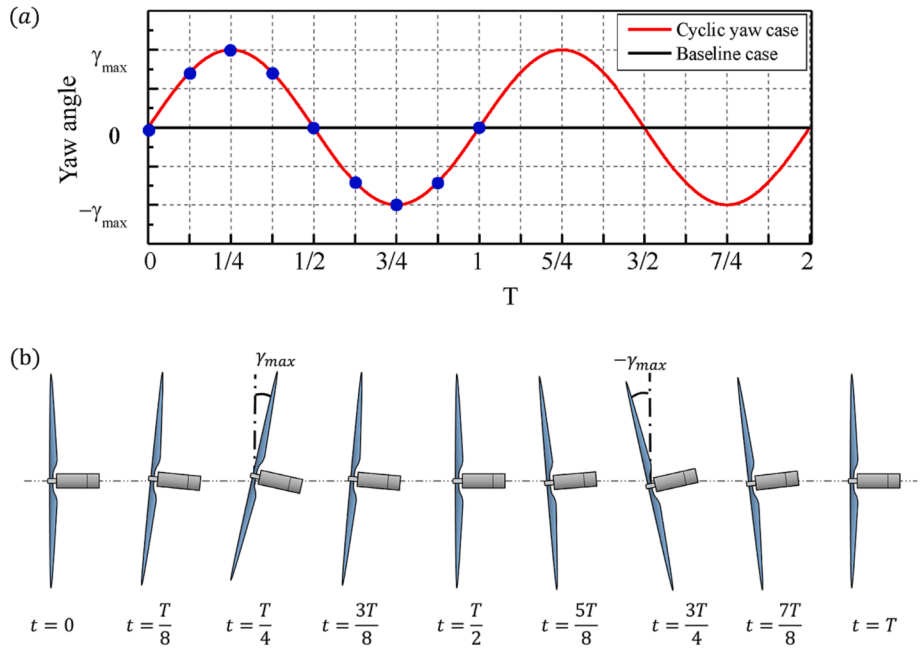

Fig. 5. Illustration of the CYC strategy: (a) time variation of yaw angle. (b) Top view of the rotor position at different time instances highlighted by blue dots in (a) during one cyclic yaw period, where $T = D/(St_y\overline{u}_{hub})$ is the cyclic yaw period.

overall flow field measured is $3D \times 15D$. The laser used in the PIV measurements is a 425 mJ dual-head Nd:YAG laser (Litron, Nano TRL 425–10). Both the camera (LaVision-sCMOS) and the optics used to generate the laser sheet are mounted on traversing beams to shift the FOVs in the streamwise direction. Tracing particles (olive-oil droplets with a diameter of about 1 μm) are seeded into the boundary layer flow from an atomizer array near the entrance of the test section. In each case, 1000 image pairs are recorded in one single FOV at a sampling frequency of 10 Hz.

The post-processing is performed in two steps of reducing size interrogation windows, where window sizes of 64 × 64 pixels and 32 × 32 pixels are used in the first and second steps, respectively. An overlap of 75 % is kept between neighboring windows and the correlation is obtained by two passes through each window size. In this study, the spatial resolution of the PIV measurements is 0.0105D.

2.4. Cyclic yaw control strategies

To apply CYC to a wind turbine, the yaw angle of the wind turbine is forced to vary cyclically. In this study, the yaw angle of T1 is varied in a sinusoidal manner (as presented in Fig. 5), while T2 and T3 are kept at zero yaw angles. The sinusoidal variation ensures a smoother transition of yaw angle especially near extrema, compared to the sawtooth, triangular or square curves. The sinusoidal variation is controlled via two parameters: the yaw angle amplitude $\gamma_{\max}$ and the yaw Strouhal number St_y, which is given by $St_y = fD/U_\infty$ (f is the yaw frequency and U_∞ is the inflow velocity, which is taken as $\overline{u}_{hub}$ in this study). The Strouhal number is a nondimensional frequency that is used to describe the periodicity in wake dynamics, such as wake meandering [27]. It should be noted that the Strouhal number has also been used as a control parameter in some previous studies on the dynamic induction control strategy (see e.g., [13]). The control formula of CYC is given as follows:

$$\gamma(t) = \gamma_{max} sin\left(2\pi \frac{St_y \overline{u}_{hub}}{D} t\right) \tag{1}$$

where $\gamma(t)$ is the instantaneous yaw angle at time t. To find the optimal control parameters for maximal wind farm power output, various combinations of γ_{max} and St_y are examined. In this study, various cases were tested with γ_{max} in the range from 0 to 35° with intervals of 5°, and St_y in the range from 0.032 to 0.32 with intervals of around 0.032. A baseline case without any cyclic yaw control is selected as a reference, which can also be interpreted as a special case where γ_{max} is zero.

3. Results and discussion

In this section, the results of power measurement and wake measurements for both the single wind turbine and the wind farm situations are presented and discussed.

3.1. Power performance of a single turbine

In the numerical simulation work of Kimura et al. [29], it is reported that CYC improves the power production of a single wind turbine. For a stand-alone wind turbine with an inflow normal to the rotor plane, being yawed at a fixed angle reduces its power output as the available energy at the rotor plane decreases. Compared to the baseline case, the normalized power production of a single wind turbine decreases when CYC is applied (see in Fig. 6). Increasing either $\gamma_{\max}$ or St_y will reduce the power output of the turbine as presented in Fig. 6(a) and (b) respectively, while the optimal TSR (λ_{opt}) remains approximately 3.6 for all the cases (the reference velocity for TSR is $\overline{u}_{hub}$). In contrast with the results reported by Kimura et al. [29], the power improvement for a stand-alone turbine under CYC is not observed in the current study for any combination of control parameters investigated.

To explain why a different result is found in this study and derive theoretically how CYC can affect the power production of the wind turbine, the power available at the rotor-swept area of the wind turbine is analyzed. For the sake of simplicity, a steady and uniform inflow velocity with a magnitude of $\overline{u}_{hub}$ is assumed. For a wind turbine at a fixed yaw angle γ the power available (P_a) to the rotor plane is $\frac{1}{2}\rho\pi R^2 \overline{u}_{hub}^3 cos^3\gamma$, where ρ is the air density. For a wind turbine under CYC, at a given time t, the available power should be calculated based on the local velocity that the rotor plane experiences, which is the resultant velocity ($u_r(t)$) of the inflow velocity and the rotor velocity due to the dynamic yaw motion, as illustrated in Fig. 7. Therefore, by integrating over the rotor plane, the available power at a given time t can be written as:

$$P_a(t) = \iint \frac{1}{2}\rho\pi R^2 [u_r(t)]^3 dS = \frac{1}{2}\rho\pi R^2 [\overline{u}_{hub} \bullet cos(\gamma(t))]^3 \bullet [1 + A(t)] \tag{2}$$

where S is the rotor-swept area and A(t) accounts for the contribution from the dynamic yaw motion, which is given by:

$$A(t) = \frac{3}{4}\left(\frac{\Omega_y(t) \bullet R}{\overline{u}_{hub} \bullet \cos(\gamma(t))}\right)^2 \tag{3}$$

where $\Omega_y(t)$ is the angular velocity of the yaw motion at time t derived from Eq. (1), which can be expressed as:

$$\Omega_y(t) = \frac{d}{dt}\gamma(t) = 2\pi \frac{St_y \overline{u}_{hub}}{D} \gamma_{max} cos\left(2\pi \frac{St_y \overline{u}_{hub}}{D} t\right) \tag{4}$$

Based on Eqs. (2) and (3), it can be concluded that, at any given time t, cyclic yawing always brings more available power to the rotor plane compared to the fixed-yaw case at a yaw angle of $\gamma(t)$ (as A(t) cannot be negative). The average available power in a cycle can therefore be written as:

$$\overline{P}_a = \frac{1}{T}\int_0^T P_a(t)dt = \frac{1}{2}\rho\pi R^2 \overline{u}_{hub}^3 \bullet (C_{sta} + C_{dyn}) \tag{5}$$

where

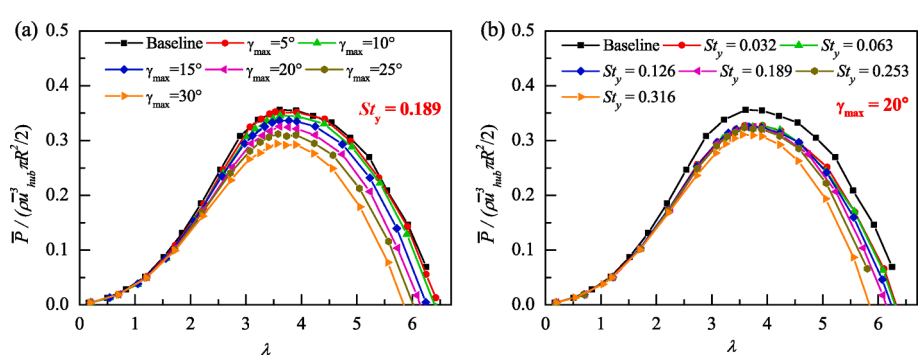

Fig. 6. Normalized power production of a single turbine under CYC as a function of TSR. (a) $St_y = 0.189$; (b) $\gamma_{\max} = 20°$.

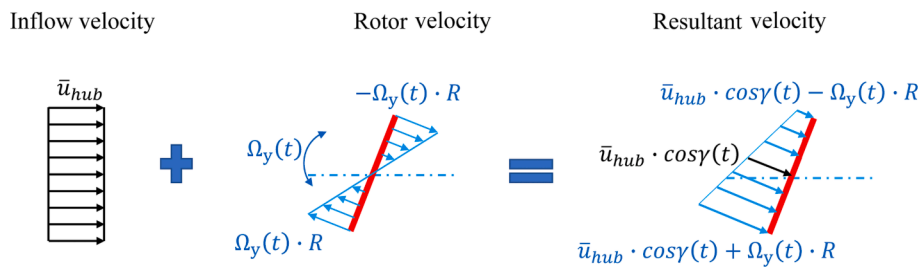

Fig. 7. The resultant velocity at the rotor plane at hub height when CYC is applied to control the turbine. The rotor plane is represented by the thick red line. Due to the cyclic yaw motion, the rotor plane itself has a velocity. At a given time *t*, the velocity at the rotor plane is the resultant velocity of the inflow velocity and the rotor velocity.

$$C_{sta}=\frac{1}{T}\int_0^T\left[cos(\gamma(t))\right]^3dt=\frac{J_0[3\gamma_{max}]+3J_0[\gamma_{max}]}{4} \tag{6}$$

is the static contribution to the available power from the inflow velocity, and

$$C_{dyn}=\frac{1}{T}\int_0^T A(t)dt=\left(\pi St_y\gamma_{max}\right)^2\bullet\frac{3}{4}\left(J_0[\gamma_{max}]-\frac{J[1,\gamma_{max}]}{\gamma_{max}}+J[2,\gamma_{max}]\right) \tag{7}$$

is the dynamic contribution from the velocity of the rotor plane induced by dynamic yawing. In Eqs. (6) and (7), $J[i,n]$ is the Bessel function of the first kind of order i with a variable n, and $J_0[n]=J[0,n]$. Bessel functions of the first kind are canonical solutions of the Bessel differential equation obtained using Frobenius' method, for more details regarding the definition and application of the Bessel function of the first kind, interested readers can refer to [33]. C_{sta} is only determined by the yaw angle amplitude (γ_{max}), while C_{dyn} is only a function of the two control parameters γ_{max} and St_y. In the expression of C_{dyn}, $\pi St_y\gamma_{max}=\frac{2\pi fR\gamma_{max}}{\bar{u}_{hub}}$ denotes a ratio between the maximum tip speed of cyclic yaw motion ($2\pi fR\gamma_{max}$) and the inflow velocity ($\bar{u}_{hub}$), which is similar to the concept of *TSR* in both vertical and horizontal axis wind turbines. In this study, it is defined as the CYC tip-speed ratio (*CYC-TSR*) and will be used for further analysis of the power performance of the turbine.

According to Eq. (5), the condition $(C_{sta}+C_{dyn})>1$ needs to be fulfilled to obtain more available power in CYC than in the zero-yaw-angle case. From Eqs. (5)–(7), a critical yaw Strouhal number (above which the rotor plane has more average available power than the zero-yaw-angle case) can be defined as:

$$St_{cri}=St_y\sqrt{\frac{1-C_{sta}}{C_{dyn}}} \tag{8}$$

For any given wind turbine size and inflow velocity, it is found that the variation of St_{cri} with γ_{max} in the range below 30° is very small. For instance, according to Eq. (8), St_{cri} slightly decreases from 0.45 to 0.43 (by 4.17 %) with the increase of the yaw angle amplitude from 0 to 30°. Therefore, it is reasonable to set $St_{cri}=0.45$ as a threshold for a wind turbine under cyclic yaw control. Moreover, the selected St_y in the study of Kimura et al. [29] is 2.22, which explains the observed power improvement as $St_y>St_{cri}$.

Substituting Eq. (8) into Eq. (5) yields a dimensionless expression of the cycle-averaged available power as follows:

$$\frac{\overline{P}_a}{\frac{1}{2}\rho\pi R^2\bar{u}_{hub}^3}=C_{sta}+C_{dyn}=St_*^2+\left(1-St_*^2\right)C_{sta} \tag{9}$$

where $St_*=St_y/St_{cri}$ is the scaled yaw Strouhal number. Since C_{sta} is only a function of γ_{max}, Eq. (9) can be used as a generalized formula for CYC for any rotor size and inflow velocity magnitude (compared with St_*, St_y still depends on R and $\bar{u}_{hub}$). Fig. 8 (a) shows the contour plot of the normalized cycle-averaged available power ($C_{sta}+C_{dyn}$) as a function of St_* and γ_{max}. At $St_*=1$, CYC brings zero gain in the available power compared to the situation when no control is applied. For $St_*<1$ a lower γ_{max} is suggested to obtain more available power, while for $St_*>1$ a higher γ_{max} is expected. This is because C_{dyn} contributes to the available power differently at $St_*<1$ and $St_*>1$. Fig. 8(b) shows the contributions of C_{sta} and C_{dyn} to the total available power of two cases with yaw frequencies below and above the critical yaw Strouhal number (i.e., $St_*=1$). According to Eq. (6), C_{sta} depends only on γ_{max} and decreases with the increase of γ_{max}, thus the variation of the available power only depends on C_{dyn} when γ_{max} is fixed. It is also found that the variation of $\frac{3}{4}\left[\left(J_0[\gamma_{max}]-\frac{J[1,\gamma_{max}]}{\gamma_{max}}+J[2,\gamma_{max}]\right)\right]$ (see in Eq. (7)) is relatively small when $\gamma_{max}\le 30°$ (dropping by only 3.41 % from $\gamma_{max}=0°$ to $\gamma_{max}=30°$), thus *CYC-TSR* ($\pi St_y\gamma_{max}$) is a dominant parameter to

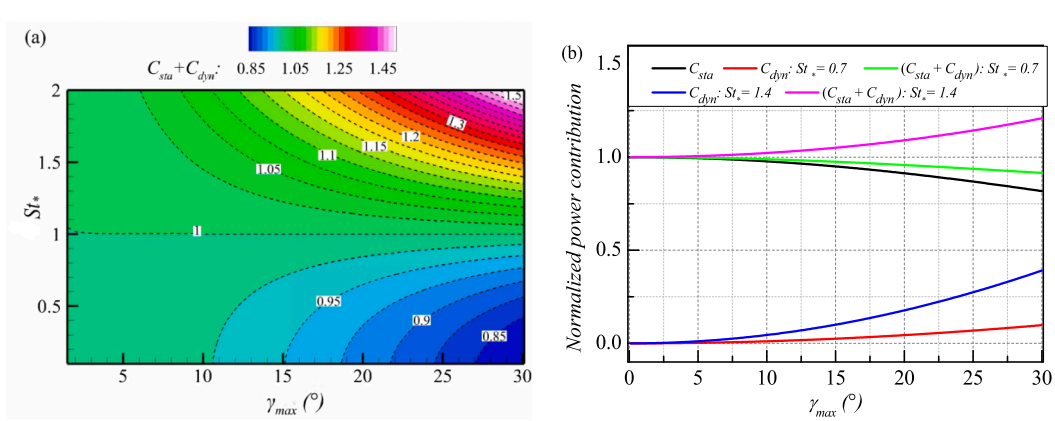

Fig. 8. Normalized cycle-averaged available power to the rotor plane: (a) contours of the available power as a function of the scaled yaw Strouhal number (St_*) and the yaw angle amplitude (γ_{max}) when CYC is applied, (b) contributions of C_{sta} and C_{dyn} when the scaled yaw Strouhal number is below and above the critical value ($St_*=1$).

determine the dynamic contribution C_{dyn} and, consequently, the variation of the available power.

While the appropriate choice of parameters can lead to more available power to the rotor plane, the real power performance of a wind turbine also depends on the aerodynamics of the rotor and the inflow conditions. Meanwhile, it is worth noting that CYC may produce high blade loads especially when operated at high yaw angle amplitudes and yaw Strouhal numbers. For practical reasons related to the blade strength (the rotor model is made of resin), the maximum yaw angle amplitude is limited to 35° in the current study, which is already an extreme value for potential engineering applications. In addition, the maximum yaw Strouhal number is limited to 0.316 for similar concerns regarding blade strength. As the maximum yaw Strouhal number is lower than the critical one ($St_{cri} = 0.45$), improving the power of a single wind turbine is not the focus of the current study. Instead, the main focus is to explore the potential of CYC in improving the power performance of a wind farm.

3.2. Power performance of the wind farm

During the power measurements, the *TSRs* of the three wind turbines are adjusted case by case to maximize the power extraction. Fig. 9 presents the dimensionless power outputs of the wind farm and individual wind turbines when CYC is applied, where the power outputs are normalized by the corresponding power outputs in the baseline case. As illustrated in Fig. 9(a), the CYC strategy can lead to the improvement of total power output within a wide range of yaw Strouhal numbers (St_y) and yaw angle amplitudes (γ_{max}) in most of the cases tested. A power gain of more than 10 % (compared to the baseline case) is found in cases with $\gamma_{max} \in (10^\circ, 35^\circ)$ and $St_y \in (0.09, 0.22)$. In the optimal case, where $(\gamma_{max}, St_y) = (20^\circ, 0.189)$, the power improvement reaches a maximum value of 15.2 %. It should be noted that this improvement is higher than the 5.4 % peak power gain achieved by Zong and Porté-Agel [9] when applying FYC to a wind farm model with the same configuration. To better understand the effects of CYC on the wind farm, the power performance of individual wind turbines is also analyzed. As presented in Fig. 9(b), the power output from the controlled turbine T1 shows high sensitivity to the variation of the yaw angle amplitude, decreasing with increasing γ_{max}, while it is found to be relatively less sensitive to the variation of the yaw Strouhal number. It can also be observed that for γ_{max} less than 25° the power extracted by T1 is more than 80 % of the power in the baseline case. The power output from the waked turbine T2 increases when γ_{max} increases as shown in Fig. 9(c), showing an opposite tendency to the power variation of T1. The power improvement of T2 can be attributed to the increased available power in the wake of T1 due to CYC [29]. The power increase of T3 shows a strong dependence on St_y as shown in Fig. 9(d), similar to the total power improvement.

Two typical scenarios, which involve fixing the yaw angle amplitude (at 20°) while varying the yaw Strouhal number, and fixing the yaw Strouhal number (at 0.189) while varying the yaw angle amplitude, are shown in Fig. 10. As shown in Fig. 10(a), the power production of T2 reaches a maximum value at $St_y = 0.189$, which is consistent with the optimal yaw Strouhal number for the maximum total power gain. For the power improvement of T3, a lower St_y is preferred. When St_y is fixed at 0.189 (as presented in Fig. 10(b)), the power of T1 decreases monotonically with the increase of γ_{max}, while T2 extracts more power. The power output of T3 reaches its peak value at $\gamma_{max} = 25^\circ$. This contributes to the decrease of the total power output when yaw angle amplitudes higher than 25° are applied, together with the power decrease of T1. To understand the mechanism of the power variation of the wind farm and individual wind turbines, further discussion on the wake characteristics is presented in section 3.3 based on the results from the PIV measurements.

Even though an improved power performance can be achieved in wind farms using CYC, this externally-driven control strategy also con-

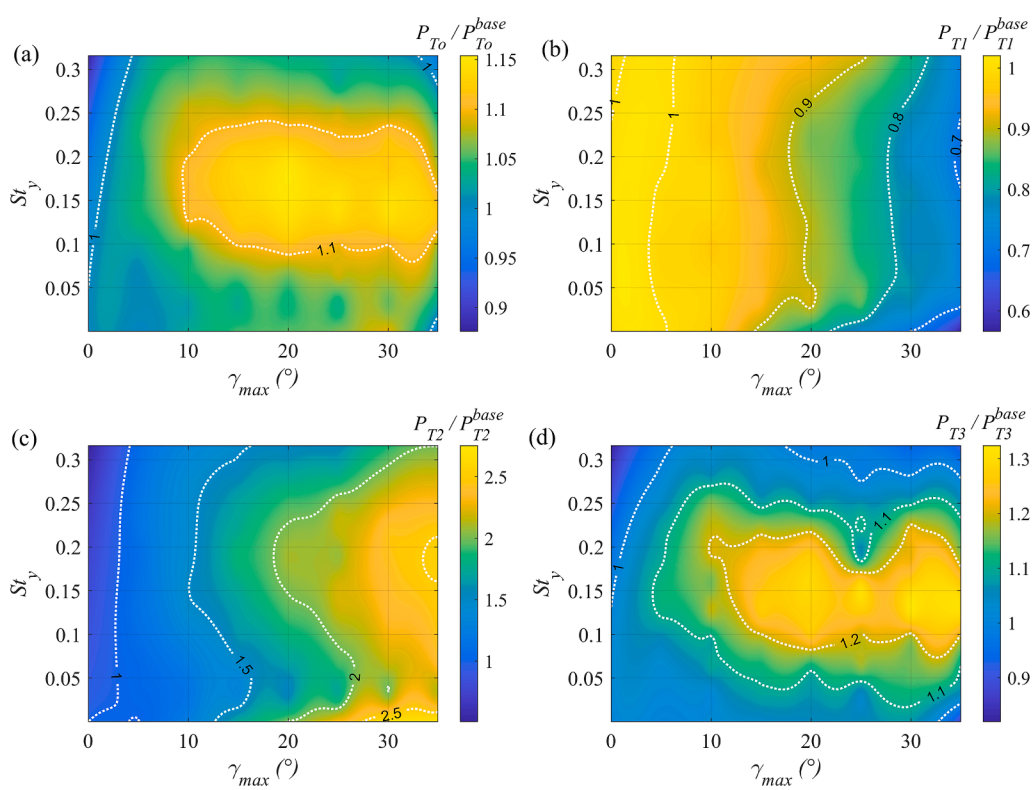

Fig. 9. Contours of the normalized power output as a function of control parameters. (a) P_{To}/P_{To}^{base}: total power of the wind farm normalized by the total power in the baseline case. (b) P_{T1}/P_{T1}^{base}. (c) P_{T2}/P_{T2}^{base}. (d) P_{T3}/P_{T3}^{base}. Note that the color bar of each subfigure is defined individually to show differences among cases more clearly.

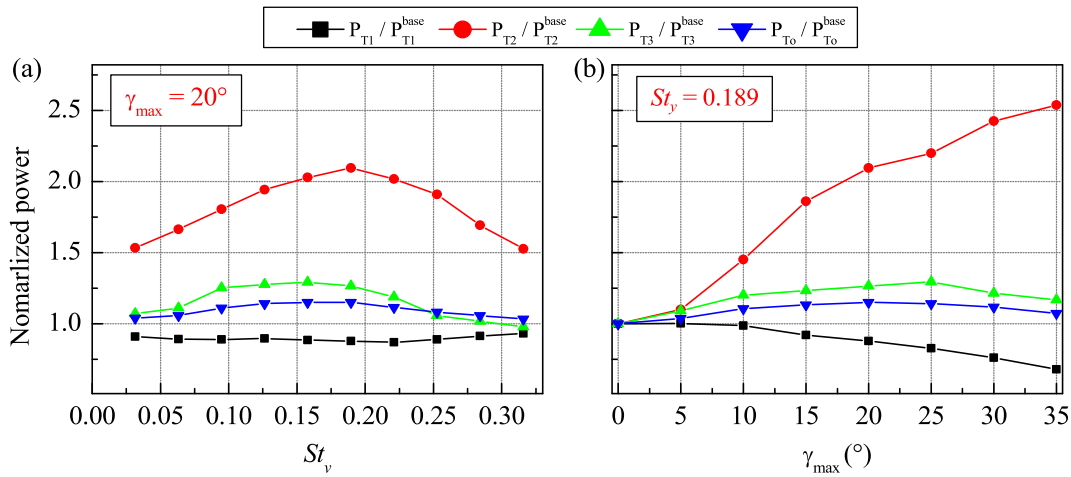

Fig. 10. Normal power production of individual wind turbines and the wind farm: (a) power variation with yaw Strouhal number at $\gamma_{max} = 20^{\circ}$; (b) power variation with yaw angle amplitude at $St_y = 0.189$.

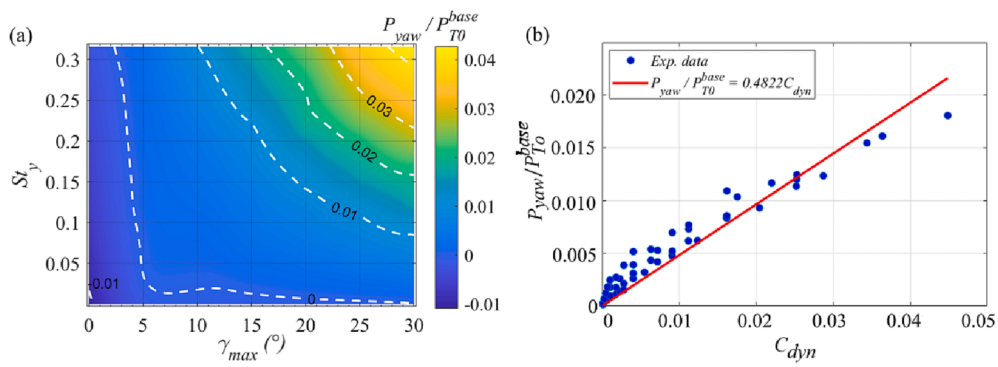

Fig. 11. Power consumed to generate CYC: (a) contours of normalized average power consumption to generate CYC as a function of control parameters; (b) P_{yaw} / P_{To}^{base} as a function of C_{dyn}, the red line shows the linear fit.

sumes power to maintain the dynamic yawing motion. To quantify the power needed to generate CYC (P_{yaw}), the electric power losses in the yaw control motor are measured. Fig. 11(a) presents the contour of P_{yaw} (normalized by the wind farm's total power production in the baseline case P_{To}^{base}) as a function of γ_{max} and St_y. Compared to the wind farm power production, the power needed to generate CYC is negligible, especially for moderate γ_{max} and St_y values. For example, for the optimal case where $(\gamma_{max}, St_y) = (20^{\circ}, 0.189)$, power consumption is about 1.3 % of the total power production in the baseline case, which still yields a net power gain of about 14 %. As P_{yaw} is consumed to generate and control the dynamic yaw motion which brings the dynamic contribution to the rotor-available power, it can be related to C_{dyn} based on Eqs. (5)–(7). One can also replace C_{dyn} with $(\pi St_y \gamma_{max})^2$ (i.e., the square of *CYC-TSR*) because $\frac{3}{4}\left(J_0[\gamma_{max}] - \frac{J[1,\gamma_{max}]}{\gamma_{max}} + J[2,\gamma_{max}]\right)$ in Eqs. (7) stays nearly constant when $\gamma_{max} \leq 30^{\circ}$, as mentioned previously. Fig. 11 (b) shows the P_{yaw}/P_{To}^{base} as a function of C_{dyn}, which indicates that the power used to generate CYC can be approximated by a linear relation as follows:

$$\frac{P_{yaw}}{P_{To}^{base}} = m \bullet C_{dyn} \tag{10}$$

In this study, m is 0.4822 for the WiRE-01 turbine based on linear fitting. It should be noted, however, that for utility wind turbines, it is necessary to measure P_{yaw} in order to know the value of m. In this context, several key differences between the laboratory setup and utility-scale turbines must be considered. For one thing, the yaw control motor of the WiRE-01 turbine is placed at the bottom of the tower, while yaw drives of utility-scale turbines are placed on top of the towers (as a result, there is no extra loading from the tower exerted on the yaw drive). In addition, utility-scale yaw drives can have very different mechanical and electrical properties compared to laboratory-scale yaw motors, which can lead to differences in the power consumption between the two.

3.3. Particle-image velocimetry measurements

To understand how CYC results in an increase in the available power for the downstream turbines, wake characteristics are investigated using PIV measurements for both a single wind turbine and the wind farm. As listed in Table 1, six cases are selected for PIV measurements, including the baseline case, which allows the study of both the effect of the yaw Strouhal number (by cases 2 – 4) and the effect of the yaw angle amplitude (by cases 1, 3 and 5) on the wake. Fig. 12 illustrates the contribution of each wind turbine to the overall power output of the

Table 1
Cases selected for PIV measurements.

Case	γ_{max}(°)	St_y	$\bar{u}_{hub}$(m/s)	λ	$\Delta P/P_{To}^{base}$
Baseline	0	–	4.75	3.6	0
Case 1	10	0.189	4.75	3.6	10.6 %
Case 2	20	0.032	4.75	3.6	4.1 %
Case 3	20	0.189	4.75	3.6	15.2 %
Case 4	20	0.253	4.75	3.6	8.3 %
Case 5	30	0.189	4.75	3.6	11.7 %

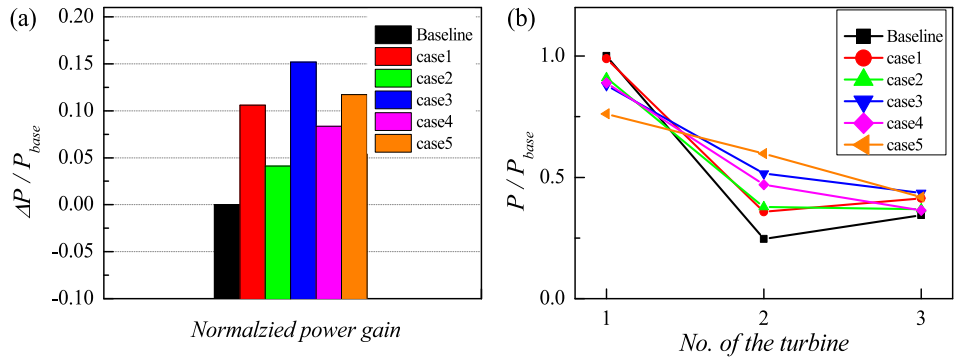

Fig. 12. Normalized power for all selected cases. (a) Normalized power gain. (b) Power contribution by each wind turbine in the wind farm for different cases. The power is normalized by the power of T1 in the baseline case.

wind farm for each case. As can be seen from Fig. 12(a), all the chosen CYC cases show a positive power gain compared to the baseline case, where the amount of gain depends on the combination of $\gamma_{\max}$ and St_y. Fig. 12(b) shows that CYC causes the decrease of the power output of T1 but improves the power production of downstream wind turbines T2 and T3, which results in an overall power gain for the wind farm. In the optimal case (case 3), although the power output of T1 is less than in the baseline case, the total power gains in T2 and T3 make it outperform other CYC cases.

3.3.1. A single turbine under cyclic yaw control

The mean streamwise velocity distributions in the wake of a single wind turbine in the baseline case and cases 1–5 are shown in Fig. 13. Comparing cases 1–5 to the baseline case, it is obvious that the wake recovers faster in the CYC cases. Comparison among cases 1, 3 and 5 reveals that increasing the yaw angle amplitude accelerates the wake recovery, while increasing the yaw Strouhal number also has similar effect based on the comparison among cases 2–4. To evaluate the influence of CYC on the wake flow, Fig. 14 presents the normalized mean streamwise wake velocity deficit profiles at various downstream positions. It can be seen that all CYC cases have lower wake velocity deficits than the baseline case at all observed downstream positions. In the proximity of the turbine, for example at x = 0.5D and x = 1D, the CYC cases have narrower wake velocity deficit profiles with a lower maximum deficit compared to the baseline case. To understand this, the overall mean wake velocity deficit of the turbine under CYC can be considered as the mean of the phase-averaged deficits (averaged at times t for which $\gamma(t)$ is the same) for all yaw angles γ within a CYC period. For simplicity, it can be assummed that the phase-averaged wake deficits can be approximated by those of turbine wakes with equivalent fixed yaw angles. The dynamic motion of the wake explains the lower velocity deficit maximum for the CYC mean wakes near the turbine compared to the baseline case. The smaller wake width (compared to the baseline case) close to the turbine can be explained by the fact that the initial wake width of a yawed turbine is less than that in the zero-yaw-angle situation [20], as the projected rotor-swept area (perpendicular to the inflow direction) is smaller. Even though cyclic yawing can cause a wake deflection in the lateral direction, the deflection is still too small near the

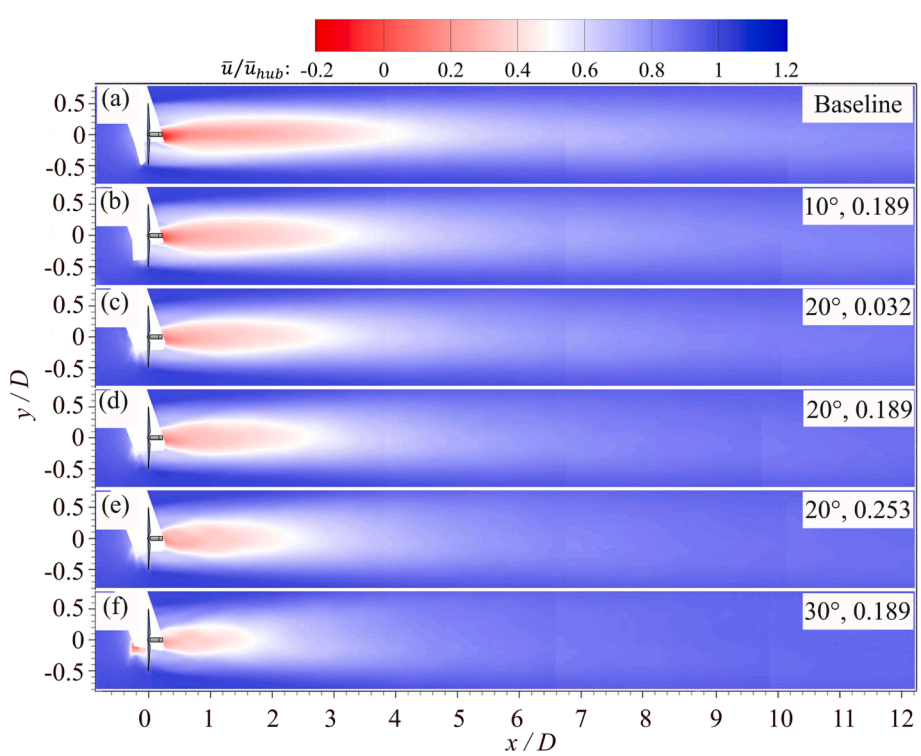

Fig. 13. Normalized mean streamwise velocity distribution in the horizontal plane at the hub height for (a) the baseline case and (b)–(e) cases 1 − 5. The control parameters of CYC are also given in the figure.

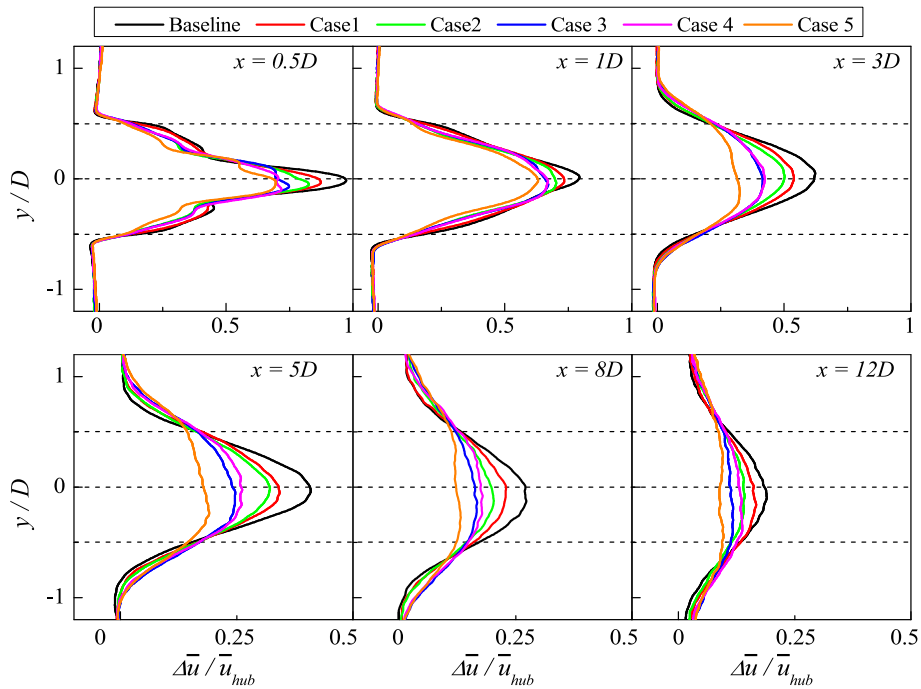

Fig. 14. Normalized mean streamwise wake velocity deficit profiles at different downstream positions in the horizontal plane at the hub height. The dashed lines denote the center line and the swept edges of the wind turbine rotor. Notice that the scale of the x-axis of the bottom figures is different from the top figures in order to clearly show the differences among cases.

rotor to result in a wake width wider than in the baseline case. Therefore, within a certain distance from the rotor, CYC cannot lead to a wider mean wake deficit profile than the baseline case. At further downstream positions (i.e., x $\geq$ 3D as shown in Fig. 14), due to the wake growth and the increasing wake deflection with the increase of x, wake profiles in CYC cases are observed to be wider than in the baseline case. It is also interesting to see that in some CYC cases, such as case 5, the velocity deficit profiles in the far wake are not completely Gaussian and even tend to exhibit two peaks (e.g., at x = 8D and x = 12D in case 5). This can be explained based on the previously mentioned consideration of the CYC mean wake as the average of several yawed wakes with different yaw angles. Since the mean wake velocity profile of a fixed yaw turbine can be approximated by a Gaussian distribution [20], the overall mean velocity profile of a turbine under CYC can be represented by the superposition of various Gaussian profiles. This can lead to an overall mean wake velocity deficit profile that is flatter or has more than one peak, compared to that of non-yawed turbines. Moreover, some profiles are less symmetrical about the wake centerline, for example, those at x = 3D and x = 5D for cases 3 and 5. This could be associated with the skewness of the yaw velocity deficit profiles [21] and the combined effects of incoming flow shear and turbine rotation.

According to Bastankhah and Porté-Agel's wake model [34], mean velocity deficit profiles in the far wake region of a stand-alone wind turbine can be reasonably represented by the self-similar Gaussian distribution. The normalized mean wake velocity deficit thus can be written as:

$$\frac{\Delta u}{u_\infty} = C(x)e^{-\frac{r^2}{2\sigma^2}} \tag{11}$$

where u_∞ is the inflow velocity, σ is the standard deviation of the Gaussian-fitted wake velocity deficit profiles at each downstream position x (i.e., the wake width), C(x) is the maximum mean wake velocity deficit at x, and r is the radial distance from the center of the wake. Based on the assumption of a linear wake growth [34], the normalized wake width σ/D can be written as:

$$\frac{\sigma}{D} = k\frac{x}{D} + \varepsilon \tag{12}$$

where k is the wake growth rate and ε is the normalized initial wake width. However, as mentioned before and as indicated in Fig. 14, mean wake velocity deficit profiles in some CYC cases do not follow the Gaussian distribution well. This is also evident from Fig. 15, which shows the goodness of fit quantified by the residuals squared (R^2). Although the mean wake velocity deficit profiles are well fitted with a Gaussian distribution in the far wake region for the baseline case, the deficit profiles in the CYC cases are not so well represented by the Gaussian distribution. This implies that, for the CYC cases, it is necessary to reconsider either the wake velocity deficit shape assumption or take the temporal variation of wake velocity deficit profiles in a cycle into account.

As the Gaussian-shaped wake velocity deficit profile assumption does not always hold in CYC cases, it is necessary to have a more generalized indicator of the wake width applicable to both the baseline case and CYC cases regardless of the shape of the wake velocity deficit profiles and the symmetry. Bastankhah and Porté-Agel [20] suggest the following equation for non-Gaussian profiles:

$$\sigma_y = \frac{1}{\sqrt{2\pi}(\overline{u}_{hub} - \overline{u}_c)} \lim_{y\to\infty} \int_{-y}^{y} (\overline{u}_{hub} - \overline{u}) d\widehat{y} \tag{13}$$

where σ_y is the wake width in the y direction, $\overline{u}_c$ is the velocity of the wake center and $\widehat{y}$ is the integration variable. Eq. (13) can be reduced to the standard deviation of the profile if it is purely Gaussian-shaped. Fig. 16 presents the nondimensional wake width as a function of downstream distance from the turbine for all the cases. It is interesting to see that, for the baseline case and the CYC cases, wake width growth can be well approximated by a linear relation with the downstream distance from the rotor plane. Higher values of k (based on Eq. (12)) are found in CYC cases than in the baseline case, indicating faster wake recovery, which is consistent with the observation from the mean wake deficits shown in Fig. 14. For cases 1, 3 and 5, which have the same yaw Strouhal number St_y of 0.189, the wake growth rate k increases with the increase

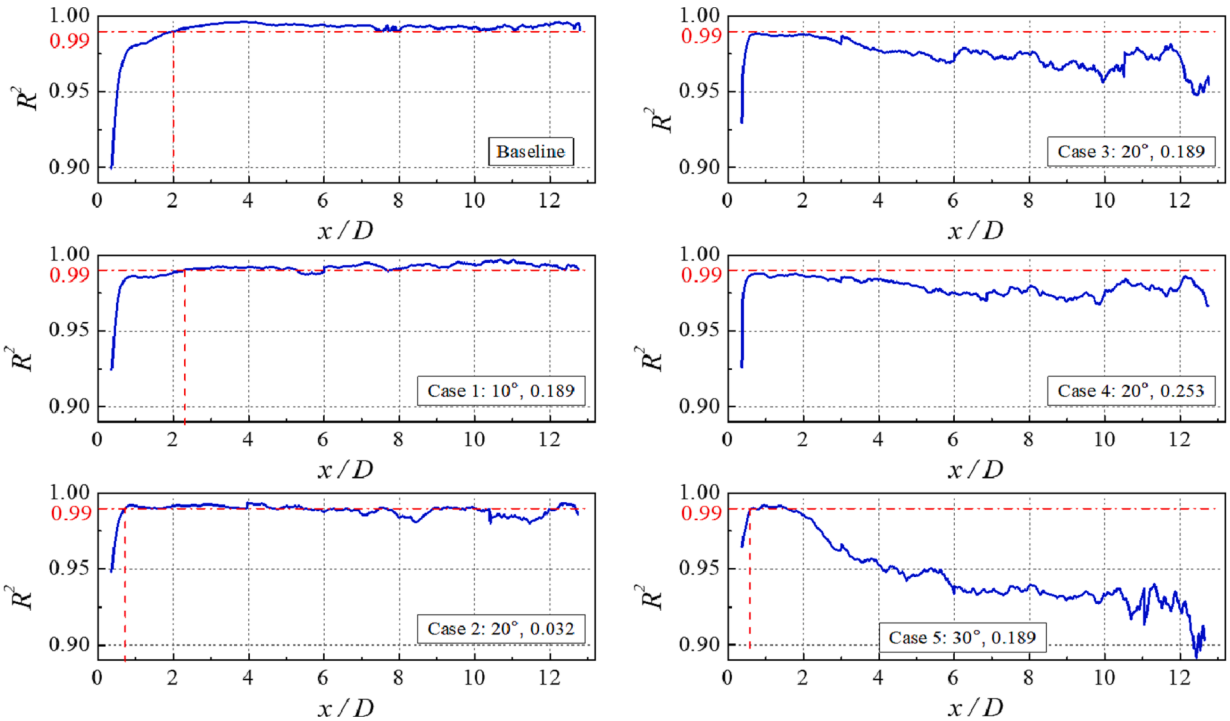

Fig. 15. Goodness of fit in the wake of the turbine when fitting a Gaussian distribution to the mean wake velocity deficit. The horizontal dash-dotted lines denote $R^2 = 99$ % and the vertical dashed lines denote the downstream position when R^2 first reaches 99 %.

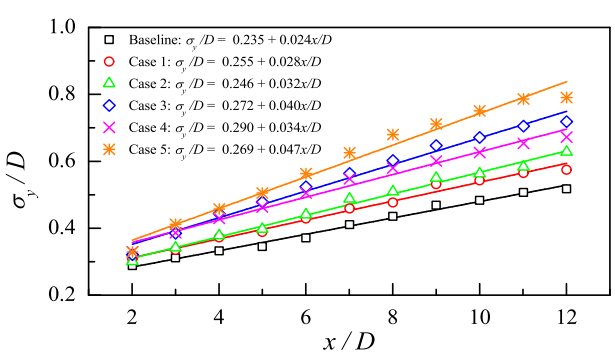

Fig. 16. Normalized wake width evaluated from Eq. (13) as a function of downstream distance for all cases. The legend shows the linear fit equations. A solid line denotes the linear fitting of the scatters in the same color.

of the yaw angle amplitude γ_{max}. This is because the wake is steered laterally to cover a larger area when γ_{max} is increased. Comparisons among cases 2 − 4, which have the same γ_{max} of 20°, indicate that the yaw Strouhal number that yields the fastest wake growth rate is $St_y = 0.189$. This shows that the wake growth rate does not increase monotonically with the increase of St_y.

When CYC is applied to the turbine, its rotor undergoes an out-of-plane cyclic yawing motion besides the in-plane rotation, which enhances the interaction between the wake and the ambient flow. Compared to the baseline case, the CYC-enhanced interaction results in different wake turbulence intensity distributions in the CYC cases. Fig. 17 presents the streamwise turbulence intensity profiles at different downstream positions at the hub-height level. At x = 0.5D, four peaks of streamwise turbulence intensity are observed for all cases due to the tip and hub annular shear layers. At shorter downstream distances (x ≤ 3D), the CYC cases show higher turbulence intensity compared to the baseline case. This can be related to the fact that the hub and tip shear layers are continuously deflected due to the dynamic yawing motion, thereby adding more fluctuations in the wake. The relatively wider turbulence intensity profiles at x = 3D for the CYC cases can also be explained by the deflection of the shear layers in the respective cases. However, at further downstream positions (e.g., x ≥ 5D), most CYC cases (except case 2) show lower turbulence intensity compared to the baseline case, especially in the rotor projected region (i.e., |y/D| ≤ 0.5). Fig. 18 more evidently shows the difference by the contours of the CYC-induced added turbulence intensity I_a^{cyc} defined as follows:

$$I_a^{cyc} = \begin{cases} -\sqrt{I_0^2 - I^2}, \, if \; I < I_0, \\ \sqrt{I^2 - I_0^2}, \, if \; I > I_0, \end{cases} \tag{14}$$

where I_0 and I are the turbulence intensity distributions of the baseline case and the CYC case respectively. I_a^{cyc} represents the added turbulence intensity contributed by the cyclic yawing motion of the wind turbine.

As presented in Fig. 18, CYC causes an increase of wake turbulence intensity by at least 10 % near the turbine location (e.g., x < 3.5D). Comparing cases 1, 3 and 5 (with the same St_y of 0.189), it is found that with the increase of γ_{max} the near-wake I_a^{cyc} increases and its maximum value appears at a position closer to the rotor plane. In cases 2 − 4 (with the same γ_{max} of 20°), it is observed that the streamwise length of the region with enhanced turbulence intensity decreases with the increase of St_y, compared with the baseline case. For case 2, wake turbulence intensity reduction is not observed, which is probably because the reduction happens at a downstream position beyond the captured FOVs. The reduction in wake turbulence intensity compared to the baseline case depends on not only the increase of St_y but also the increase of γ_{max}, as illustrated in Fig. 18. This indicates that CYC has the potential to reduce the turbulence-induced unsteady forcing on the downstream wind turbines as well. It is also found that, although the far-wake turbulence intensity in the rotor projected region is lower than in the baseline case, the turbulence intensity in the outer region (|y/D| > 0.5) is higher.

It is worth mentioning here that turbulence intensity is based on the

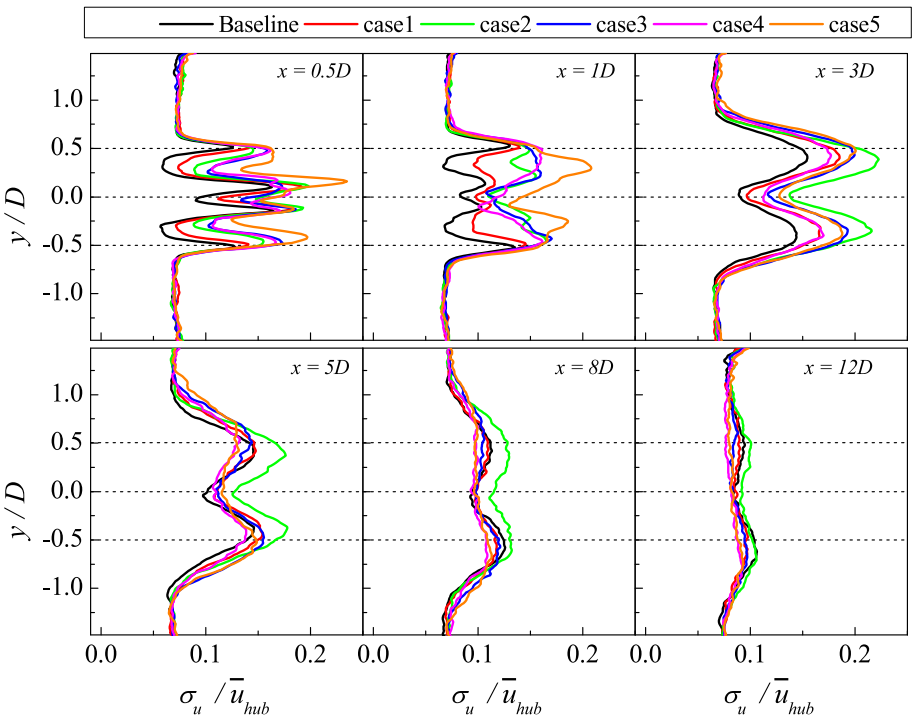

Fig. 17. Profiles of streamwise turbulence intensity at different downstream positions in the horizontal plane at the hub height. The dashed lines denote the center line and the swept edges of the wind turbine rotor.

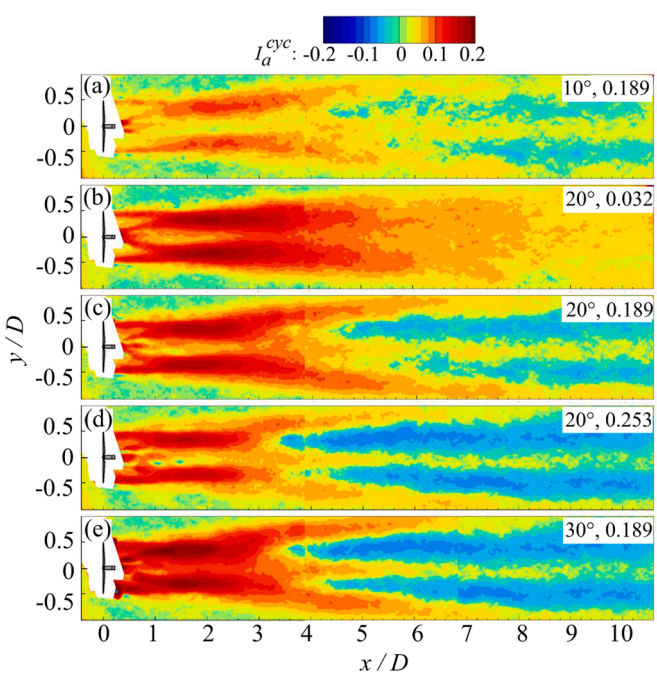

Fig. 18. Contours of the CYC-induced turbulence intensity in the horizontal plane at the hub height. Sub-figures from (a) to (e) correspond to cases 1–5. The white regions in the figure are masked regions with no values.

Reynolds decomposition, i.e., $u(t) = \overline{u} + u'$, where $\overline{u}$ is the time-averaged velocity and u' is the velocity fluctuation. For CYC, the wake dynamics are periodic and, thus the fluctuating part u' can be decomposed into a periodic term $\widetilde{u}$ and a turbulent term u'', i.e., $u' = \widetilde{u} + u''$, which was proposed by Hussain and Reynolds [35] in their study on the organized wave. In such a case, wake turbulent intensity distributions in the CYC cases are not only contributed by the turbulent fluctuations but also dependent on the periodic variations. In particular, considering a non-turbulent wake that is deflected cyclically, even without the contribution of turbulent fluctuations, the periodic variation of wake velocity can still lead to non-zero turbulence intensity in terms of statistics. This explains why different (from the baseline case) wake turbulence intensity distributions are observed in the CYC cases.

3.3.2. Cyclic yaw control in a simple wind farm model

As detailed in the aforementioned PIV results of a single wind turbine wake, applying CYC results in distributions of velocity and turbulence intensity in the turbine wake different from the baseline case, which consequently affects the power performance of downstream wind turbines. To relate the power performance of the wind farm with CYC, the wake flow of a simple wind farm model under different CYC conditions is presented and analyzed in this section. Fig. 19 shows the mean streamwise wake velocity distribution for the baseline case and all CYC cases. Akin to the wake flow of a single wind turbine, CYC accelerates the wake recovery of T1. This acceleration effect is more significant, especially in the cases with higher yaw angle amplitudes and higher yaw Strouhal numbers. Moreover, in the CYC cases, the wake recovery of downstream wind turbines is also faster compared to the baseline case, which is consistent with the differences in power performance. To elaborate on the differences in wake recovery induced by CYC, Fig. 20 presents the decay of the maximum mean streamwise wake velocity deficits for all cases investigated. The slight increase of the wake velocity deficit in front of T2 (x = 5D) and T3 (x = 10D) is due to the blockage or induction effect of the respective turbine. For all CYC cases, the maximum velocity deficit in the wake regions of all three wind turbines is smaller than the baseline case, which indicates that CYC induces faster wake recovery for not only the upstream wind turbine under control but also the downstream wind turbines. A smaller maximum velocity deficit in the wake means more available power for the downstream wind turbines. Fig. 20 also indicates that for downstream wind turbines, the differences in the decay of the maximum wake velocity deficit among various cases get smaller. However, this does not mean that the effects of CYC will vanish further downstream. This can be

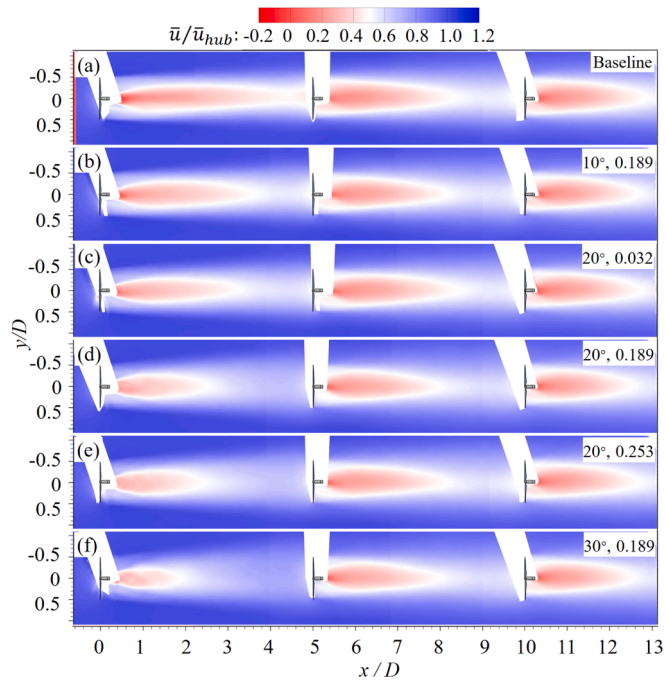

Fig. 19. Contours of normalized mean streamwise velocity in the wind farm in the horizontal plane at hub height for (a) the baseline case, and (b)–(f) CYC cases 1 – 5.

related to the fact that, for CYC cases, the far-wake velocity deficit profiles are flatter (see in Fig. 14) and the turbulence intensity level is lower in the rotor projected region and higher in the outer region (as indicated in Fig. 18), compared to the baseline case. It can also be seen from Fig. 20 that case 3 outperforms other cases in power improvement because all three wind turbines have relatively faster wake recovery. It is worth noting that, while only the first turbine is yawed cyclically, the downstream turbines are facing the cyclically yawed wake, which can be considered equivalent to applying CYC to downstream turbines.

To see the effects of CYC on the wake turbulence intensity, the distribution of CYC-induced added turbulence (I_a^{cyc}, see the definition in Eq. (14)) in the wind farm is also shown in Fig. 21. Compared to the baseline case, it is observed that in the CYC cases (except for case 2) the turbulence intensity in the wakes of T2 and T3 is higher near the wake centerline but lower near y / D = ± 0.5. Differences are found in case 2, where turbulence intensity in the center wake region of T2 and T3 is slightly smaller than in the baseline case due to the presence of downstream wind. Compared to the baseline case, Fig. 21 also shows that CYC produces higher turbulence intensity in wind farm wake flows in the region of |y/D| > 0.5. This is due to the fact that the wake of turbine T1 is continuously steered laterally via dynamic yawing and the effects extend downstream. As explained previously, the downstream turbines can be considered to have an inflow of cyclically varying directions, which consequently leads to the cyclic lateral deflection of their wakes.

3.4. Cyclic yaw control in utility-scale wind farms

The current work is based on wind tunnel experiments, where the CYC parameters are chosen based on the kinematics of the miniature wind turbines. In this section, an approximate relation for the CYC parameters that would be needed in utility-scale wind farms is proposed based on the scaling considerations used in the wind tunnel. The situation of applying CYC to a single turbine is first considered. In order to keep the kinematic similarity, it is necessary to respect the kinematic scaling between the miniature wind turbine and the utility-scale one. In general, the rotor kinematic similarity between utility-scale and miniature wind turbines (assuming the same rotor geometry details) is kept by ensuring the geometric similarity of the velocity triangles at the homologous blade sections of turbines of different scales, which can often be realized by using similar *TSR*s. However, for CYC the rotor of the controlled turbine undergoes an out-of-plane yawing motion, which adds another CYC-induced velocity component to the blade element, as illustrated in Fig. 22. In order to keep the similarity of rotor aerodynamics of two different scale turbines under CYC (only the same yaw angle amplitude for these two turbines is considered in this study), at the same phase of cyclic yawing, the following relations between different velocity components should be respected:

$$\begin{cases} \dfrac{\Omega_1 \bullet R_1}{U_{\infty,1}} = \dfrac{\Omega_2 \bullet R_2}{U_{\infty,2}} \Leftrightarrow \lambda_1 = \lambda_2, \\ \dfrac{\Omega_{y,1}(t) \bullet R_1}{U_{\infty,1}} = \dfrac{\Omega_{y,2}(t) \bullet R_2}{U_{\infty,2}} \Leftrightarrow St_{y,1} = St_{y,2}, \\ \dfrac{\Omega_1 \bullet R_1}{\Omega_{y,1}(t) \bullet R_1} = \dfrac{\Omega_2 \bullet R_2}{\Omega_{y,2}(t) \bullet R_2} \Leftrightarrow \dfrac{\Omega_1}{f_1} = \dfrac{\Omega_2}{f_2}, \end{cases} \tag{15}$$

where the subscripts '1′ and '2′ denote two turbines of different scales. Eq. (15) can be interpreted as follows: to keep the kinematic similarity between the two turbines, λ (*TSR*), St_y (the yaw Strouhal number) and Ω/f should all be the same. Ω/f represents the number of rotor revolutions per cycle of yawing, which is chosen as a control parameter in the study of Kimura et al. [29] on a single wind turbine.

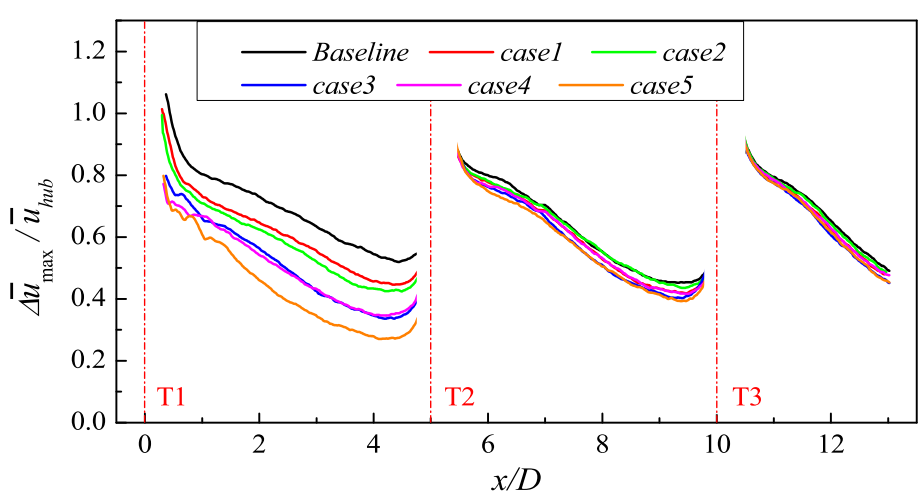

Fig. 20. Decay of the maximum mean streamwise wake velocity deficit.

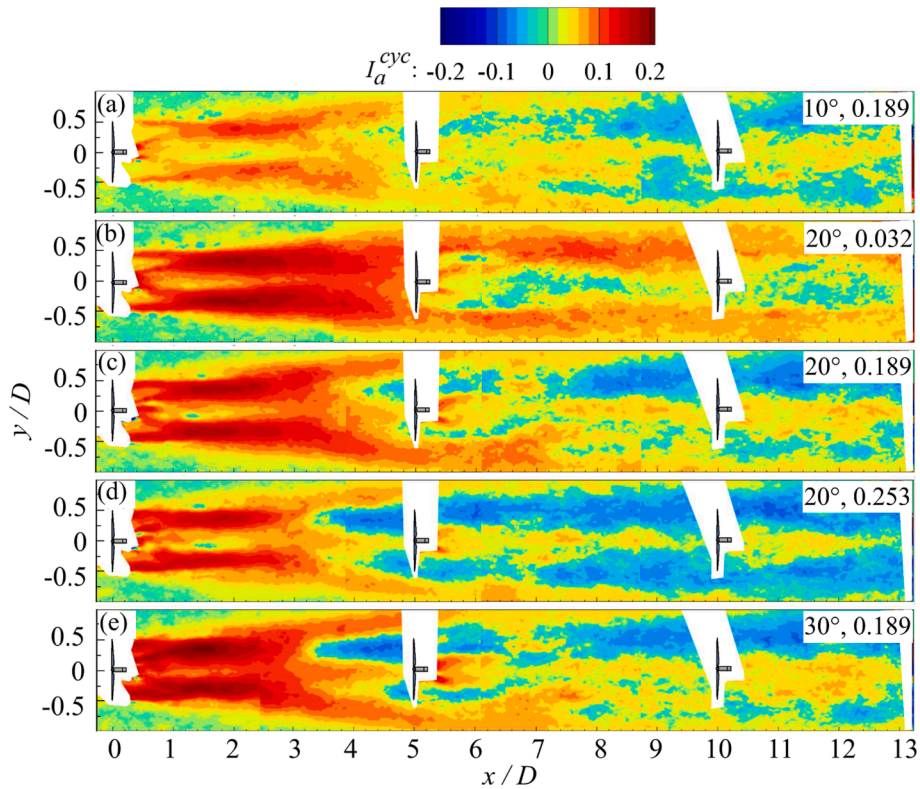

Fig. 21. Contours of the CYC-induced added wake turbulence intensity in the horizontal plane at hub height. Sub-figures from (a) to (e) correspond to cases 1–5. The white regions in the figure are masked regions with no values.

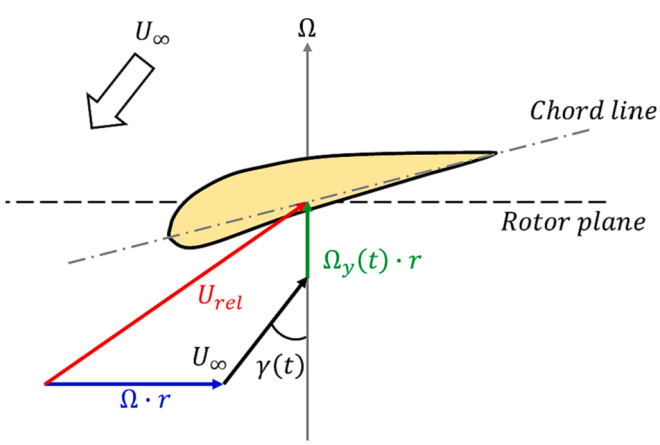

Fig. 22. A schematic of the blade element at a distance *r* from the rotor center at the time *t* during CYC.

Note that:

$$\mathrm{St}_y = 2\lambda \Big/ \left(\frac{\Omega}{f}\right) \tag{16}$$

thus the kinematic similarity can be respected by keeping the same values of any two of the three parameters: λ, St_y and Ω/f. However, as small-scale turbines can be designed with different blade configurations and slightly smaller optimal *TSRs* to have power and thrust coefficients comparable with the utility-scale ones [36], the strict similarity between wind-tunnel scale and utility-scale turbines based on Eqs. (15) and (16) may not be possible. Considering this, a compromise on λ to have comparable power and thrust coefficients is reasonable as the main focus is the power performance.

In the context of applying CYC to wind farms, as only the most upwind turbine is under control in the current study, the performance of downstream wind turbines and, consequently, the overall performance of the wind farm is mostly dependent on the wake dynamics of the controlled turbine. For wind turbines of different scales, comparable thrust coefficients ensure similar magnitudes of the normalized wake deficits (by the inflow velocity) in their far wakes, based on momentum conservation [34]. Strict scaling based on λ can be relaxed as the far wake is not substantially affected by the helicoidal vortices shed from the blade tips. Therefore, wake similarity for wind turbines of different scales under CYC control mainly depends on the similarity of wake kinematics (i.e., wake meandering motion), which can be respected by using the same or similar yaw Strouhal number St_y. Based on Eq. (15), for a utility-scale wind farm with the same layout as the wind farm model in this study, considering the typical values of $\lambda = 7$ and $\Omega = 12.1$rpm (e.g., the NREL-5 MW wind turbine at the rated wind speed [37]) for the wind turbine under control, the corresponding optimal control parameters would be $\gamma_{\max} = 20^\circ$ and $f = 0.017$Hz (i.e., $\mathrm{St}_y = 0.189$). For engineering application in utility-scale wind turbines, tests on CYC control parameters are suggested. However, the similarity consideration can be used to reasonably provide reference values of control parameters.

4. Summary

To mitigate the power losses due to wake effects in wind farms, the potential of the cyclic yaw control (CYC) strategy is investigated via wind-tunnel experiments for the first time. The experiments are carried out on a single wind turbine model and a three-turbine wind farm model in full wake state. In this strategy, the yaw angle of the most upwind turbine is varied in a sinusoidal manner, where the two control parameters are the yaw angle amplitude (γ_m) and yaw Strouhal number (St_y). The main conclusions are summarized as follows:

(1) A generalized formula for the available power to a turbine under cyclic yawing is derived based on the assumption of a steady and uniform inflow, which indicates that it is possible for a turbine under cyclic yawing to have more available power than the fixed-yaw and zero-yaw scenarios when $St_y > 0.45$.
(2) The maximum power improvement of 15.2 % appears at $St_y = 0.189$ and $\gamma_{max} = 20^\circ$, which is much higher than the 5 % peak power gain when using the fixed yaw control strategy. In general, power gains of more than 10 % can be achieved for St_y in the range of 0.09 - 0.22 and γ_{max} in the range of 10°- 30°.
(3) Wake results from a single wind turbine show that CYC can significantly enhance wake recovery. For example, in the optimal control case, the maximum wake velocity deficit at x = 5D is less than 40 % of what is in the baseline case. The wake recovery rate can be increased by either increasing the yaw Strouhal number or the yaw angle amplitude.
(4) CYC can lead to an increase in wake turbulence intensity (of around 10 − 20 %) in the proximity to the turbine, it also results in a reduction in wake turbulence intensity (of around 5 − 10 %) in the rotor projected region beyond a certain downstream distance (which is dependent on the yaw Strouhal number). This reduction in turbulence intensity indicates that CYC can potentially mitigate fatigue loading on downstream wind turbines.
(5) To achieve similar power gain (in percentage) in utility-scale wind farms, it is suggested to keep a similar yaw Strouhal number as in small-scale wind farms, based on kinematic similarity considerations. The typical value of optimal yaw frequency is estimated to be around 0.017 *Hz* (i.e., $St_y = 0.189$), taking the NREL-5 MW wind turbine as an example.

This study proves the great potential of applying the CYC strategy in wind farms. However, some open issues still need to be further explored. For instance, it is essential to investigate the impacts of the CYC strategy on the loading of wind turbines. The potential of CYC should also be verified through numerical simulations and field measurements on utility-scale wind turbines. In addition, the power and wake benefits of CYC can also be investigated in wind farms with different layouts and in different inflow conditions such as different wind directions, turbulence intensity and thermal stability.

CRediT authorship contribution statement

Guiyue Duan: Conceptualization, Methodology, Investigation, Data curation, Formal analysis, Writing – original draft, Visualization. **Arslan Salim Dar:** Conceptualization, Methodology, Investigation, Writing – review & editing. **Fernando Porté-Agel:** Conceptualization, Methodology, Supervision, Resources, Writing – review & editing, Funding acquisition.

Declaration of Competing Interest

The authors declare that they have no known competing financial interests or personal relationships that could have appeared to influence the work reported in this paper.

Data availability

Data will be made available on request.

Acknowledgements

This work is funded by the European Union Horizon 2020 research and innovation program, Train2Wind project, grant agreement no. 861291. The authors also acknowledge the support from the Swiss National Science Foundation (Grant Number: 200021_215288) and the Swiss Federal Office of Energy (Grant No. SI/502135–01).

References

[1] Nash R, Nouri R, Vasel-Be-Hagh A. Wind turbine wake control strategies: A review and concept proposal. Energy Convers Manag 2021;245:114581. https://doi.org/10.1016/J.ENCONMAN.2021.114581.
[2] Barthelmie RJ, Folkerts L, Larsen GC, Rados K, Pryor SC, Frandsen ST, et al. Comparison of wake model simulations with offshore wind turbine wake profiles measured by Sodar. J Atmos Ocea Technol 2006;23:888–901. https://doi.org/10.1175/JTECH1886.1.
[3] F. Porté-Agel, M. Bastankhah, S. Shamsoddin, Wind-turbine and wind-farm flows: A review, Boundary-Layer Meteorol 2019 174:1. 174 (2019) 1–59. 10.1007/S10546-019-00473-0.
[4] Gualtieri G. A novel method for wind farm layout optimization based on wind turbine selection. Energy Convers Manag 2019;193:106–23. https://doi.org/10.1016/J.ENCONMAN.2019.04.059.
[5] Yang Q, Li H, Li T, Zhou X. Wind farm layout optimization for levelized cost of energy minimization with combined analytical wake model and hybrid optimization strategy. Energy Convers Manag 2021;248:114778. https://doi.org/10.1016/J.ENCONMAN.2021.114778.
[6] Bai F, Ju X, Wang S, Zhou W, Liu F. Wind farm layout optimization using adaptive evolutionary algorithm with Monte Carlo Tree Search reinforcement learning. Energy Convers Manag 2022;252:115047. https://doi.org/10.1016/J.ENCONMAN.2021.115047.
[7] Bastankhah M, Porté-Agel F. Wind farm power optimization via yaw angle control: A wind tunnel study. J Renew Sustain Energy 2019;11:023301. https://doi.org/10.1063/1.5077038.
[8] Song D, Yang J, Fan X, Liu Y, Liu A, Chen G, et al. Maximum power extraction for wind turbines through a novel yaw control solution using predicted wind directions. Energy Convers Manag 2018;157:587–99. https://doi.org/10.1016/J.ENCONMAN.2017.12.019.
[9] Zong H, Porté-Agel F. Experimental investigation and analytical modelling of active yaw control for wind farm power optimization. Renew Energy 2021;170:1228–44. https://doi.org/10.1016/J.RENENE.2021.02.059.
[10] Cossu C. Evaluation of tilt control for wind-turbine arrays in the atmospheric boundary layer. Wind Energy Science 2021;6:663–75. https://doi.org/10.5194/WES-6-663-2021.
[11] Dilip D, Porté-Agel F. Wind turbine wake mitigation through blade pitch offset. Energies 2017;10:757. https://doi.org/10.3390/EN10060757.
[12] van der Hoek D, Kanev S, Allin J, Bieniek D, Mittelmeier N. Effects of axial induction control on wind farm energy production - A field test. Renew Energy 2019;140:994–1003. https://doi.org/10.1016/J.RENENE.2019.03.117.
[13] Munters W, Meyers J. Towards practical dynamic induction control of wind farms: Analysis of optimally controlled wind-farm boundary layers and sinusoidal induction control of first-row turbines. Wind Energy Sci 2018;3:409–25. https://doi.org/10.5194/WES-3-409-2018.W.
[14] Alexis Frederik J, Weber R, Cacciola S, Campagnolo F, Croce A, Bottasso C, van Wingerden JW. Periodic dynamic induction control of wind farms: Proving the potential in simulations and wind tunnel experiments. Wind Energy Sci 2020;5:245–57. https://doi.org/10.5194/WES-5-245-2020.
[15] Lin M, Porté-Agel F. Power maximization and fatigue-load mitigation in a wind-turbine array by active yaw control: an LES study. J Phys Conf Ser 2020;1618:042036. https://doi.org/10.1088/1742-6596/1618/4/042036.
[16] Jiménez Á, Crespo A, Migoya E. Application of a LES technique to characterize the wake deflection of a wind turbine in yaw. Wind Energy 2010;13:559–72. https://doi.org/10.1002/WE.380.
[17] Bartl J, Mühle F, Sætran L. Wind tunnel study on power output and yaw moments for two yaw-controlled model wind turbines. Wind Energy Sci 2018;3:489–502. https://doi.org/10.5194/WES-3-489-2018.
[18] Fleming P, Annoni J, Shah JJ, Wang L, Ananthan S, Zhang Z, et al. Field test of wake steering at an offshore wind farm. Wind Energy Sci 2017;2:229–39. https://doi.org/10.5194/WES-2-229-2017.
[19] N.O. Jensen, A Note on Wind Generator Interaction, 1983.
[20] Bastankhah M, Porté-Agel F. Experimental and theoretical study of wind turbine wakes in yawed conditions. J Fluid Mech 2016;806:506–41. https://doi.org/10.1017/JFM.2016.595.
[21] Dou B, Guala M, Lei L, Zeng P. Wake model for horizontal-axis wind and hydrokinetic turbines in yawed conditions. Appl Energy 2019;242:1383–95. https://doi.org/10.1016/J.APENERGY.2019.03.164.
[22] Lopez D, Kuo J, Li N. A novel wake model for yawed wind turbines. Energy 2019;178:158–67. https://doi.org/10.1016/J.ENERGY.2019.04.120.
[23] Zong H, Porté-Agel F. A point vortex transportation model for yawed wind turbine wakes. J Fluid Mech 2020;890. https://doi.org/10.1017/JFM.2020.123.
[24] Bastankhah M, Shapiro CR, Shamsoddin S, Gayme DF, Meneveau C. A vortex sheet based analytical model of the curled wake behind yawed wind turbines. J Fluid Mech 2022;933. https://doi.org/10.1017/JFM.2021.1010.
[25] R.J.A.M. Stevens, C. Meneveau, Flow Structure and Turbulence in Wind Farms, Doi.Org/10.1146/Annurev-Fluid-010816-060206. 49 (2017) 311–339, doi: 10.1146/ANNUREV-FLUID-010816-060206.
[26] España G, Aubrun S, Loyer S, Devinant P. Spatial study of the wake meandering using modelled wind turbines in a wind tunnel. Wind Energy 2011;14:923–37. https://doi.org/10.1002/WE.515.
[27] Yang X, Sotiropoulos F. A review on the meandering of wind turbine wakes. Energies 2019;12:4725. https://doi.org/10.3390/EN12244725.
[28] Munters W, Meyers J. Dynamic strategies for yaw and induction control of wind farms based on large-eddy simulation and optimization. Energies 2018;11:177. https://doi.org/10.3390/EN11010177.

[29] Kimura K, Iida M, Tanabe Y, Matsuo Y. Forced wake meandering for rapid recovery of velocity deficits in a wind turbine wake. AIAA Scitech 2019 Forum 2019. https://doi.org/10.2514/6.2019-2083.
[30] Bastankhah M, Porte-Agel F. Wind tunnel study of the wind turbine interaction with a boundary-layer flow: Upwind region, turbine performance, and wake region. Phys Fluids 2017;29:065105. https://doi.org/10.1063/1.4984078.
[31] R.B. Stull, An introduction to boundary layer meteorology, An Introduction to Boundary Layer Meteorology, 1988, doi: 10.1007/978-94-009-3027-8/COVER.
[32] Bastankhah M, Porté-Agel F. A new miniature wind turbine for wind tunnel experiments. Part I: Design and performance. Energies 2017;10:908. https://doi.org/10.3390/EN10070908.
[33] Temme NM. Special functions: an introduction to the classical functions of mathematical physics. John Wiley & Sons; 1996.
[34] Bastankhah M, Porté-Agel F. A new analytical model for wind-turbine wakes. Renew Energy 2014;70:116–23. https://doi.org/10.1016/J.RENENE.2014.01.002.
[35] Hussain AKMF, Reynolds WC. The mechanics of an organized wave in turbulent shear flow. J Fluid Mech 1970;41:241–58. https://doi.org/10.1017/S0022112070000605.
[36] Bottasso CL, Campagnolo F. Wind Tunnel Test Wind Turbines Farms 2021. https://doi.org/10.1007/978-3-030-05455-7_54-1.
[37] Jonkman J, Butterfield S, Musial W, Scott G. Definition of a 5-MW Reference Wind Turbine for Offshore System Development. 2009. https://doi.org/10.2172/947422.